

# Design and Fabrication of Suspended Indium Phosphide Waveguides for MEMS-Actuated Optical Buffering

Wing H. Ng, Nina Podoliak, Peter Horak, Jiang Wu, Huiyun Liu, William J. Stewart,  
and Anthony J. Kenyon, *Senior Member, IEEE*

**Abstract**—We present the design and fabrication of suspended optical waveguides on indium phosphide platform for use in an optical buffer device with MEMS actuation, in which the optical delay can be achieved by changing the spacing of the waveguides by electrostatic actuation. The optical and mechanical properties of the waveguides and pillar supports are modeled, and different MEMS actuation schemes are simulated. We also present fabrication and characterization results of the epitaxially grown sample structure and of the suspended waveguide device, exhibiting two parallel waveguides with submicron dimensions separated by a 400-nm air gap, and suspended at 40- $\mu\text{m}$  intervals by S-shaped supports.

**Index Terms**—III-V semiconductor materials, indium phosphide, microelectromechanical systems, optical buffering, optical waveguides.

## I. INTRODUCTION

OPTICAL buffering is one of the key functionalities required for the realization of all-optical telecommunication networks. The main function of an optical buffer is to retain data in an optical format for a desired period of time, without the need to convert them into electrical signals. One of the most common ways of achieving optical delay is by using different fiber lengths [1], however, this method can only offer discrete delay times and hence it is not flexible. Some flexibility can be achieved by switching between a range of different delay lines, but at the cost of increasingly bulky and complex devices. Another method is the use of optical resonators [2]. Although resonators can produce significant delays in a very compact package, they are limited in operating bandwidth. Similarly, slow light buffers based on electromagnetically induced transparency [3], [4] can provide large delays over a very narrow bandwidth only. In our previous work, we proposed and investigated

theoretically the possibility of achieving tunable optical delay over the whole C-band of communication wavelengths by using two parallel suspended waveguides [5] on a silicon chip.

Fabrication of freestanding optical waveguides with electro-mechanical structure was reported using silicon [6]–[8] and III-V semiconductors [9]. Compared to silicon-based materials, III-V materials such as InP and GaAs have some major advantages. In particular, these materials have a direct bandgap, which means optical gain can be achieved. It is also possible to tailor the optical emission properties of such materials by varying their compositions. From a technological point of view, lasers and other optical components for optical communications are well established in the InP platform [10]–[12], and hence monolithically integrating an optical buffer device into the same circuit would present a significant advantage.

In this paper, we thus present how such a device can be realized practically in InP. We design the optical buffer device by modeling its optical and mechanical properties, including the waveguides and pillar supports for suspension, and investigate options for MEMS actuation. Fabrication techniques for making the device are also discussed and, finally, we present the first fabrication of an InP-based device with long (200  $\mu\text{m}$ ) suspended dual waveguides of submicron dimensions with submicron separation.

## II. BUFFER OPERATION PRINCIPLE

The schematic design of our optical buffer device is shown in Fig. 1. The figure indicates the three main components of the buffer: (i) optical waveguides, (ii) pillars for the waveguide support, and (iii) electrodes for the buffer actuation. The optical part of the buffer consists of two rectangular waveguides made of high index material (InP) and surrounded by air as shown in the inset. The waveguides have subwavelength dimensions (height  $h$  and width  $w$ ) and are strongly coupled through a small air gap  $g$ , such that they support only the two fundamental symmetric TE and TM optical modes. Here, we denote by TE the mode with polarization predominantly along the major axis of the individual waveguides for  $h > w$ , and by TM the mode with orthogonal polarization. Here we design a device operating in the TE mode (see insets in Fig. 2). A detailed discussion of a buffer operating in TM mode can be found in [5].

The waveguides are suspended by pillars connected to the side as shown in Fig. 1. The waveguides are straight and

Manuscript received October 1, 2014; revised November 16, 2014 and December 11, 2014; accepted December 14, 2014. This work was supported by the Engineering and Physical Sciences Research Council under Grants EP/J012823/1 and EP/J012874/1.

W. H. Ng, J. Wu, H. Liu, and A. J. Kenyon are with the Department of Electronic and Electrical Engineering, University College London, London WC1E 7JE, U.K. (e-mail: w.ng@ucl.ac.uk; jiang.wu@ucl.ac.uk; huiyun.liu@ucl.ac.uk; a.kenyon@ucl.ac.uk).

N. Podoliak, P. Horak, and W. J. Stewart are with the Optoelectronics Research Centre, University of Southampton, Southampton SO17 1BJ, U.K. (e-mail: n.podoliak@soton.ac.uk; peh@orc.soton.ac.uk; w.j.stewart@soton.ac.uk).

Color versions of one or more of the figures in this paper are available online at <http://ieeexplore.ieee.org>.

Digital Object Identifier 10.1109/JSTQE.2014.2384514

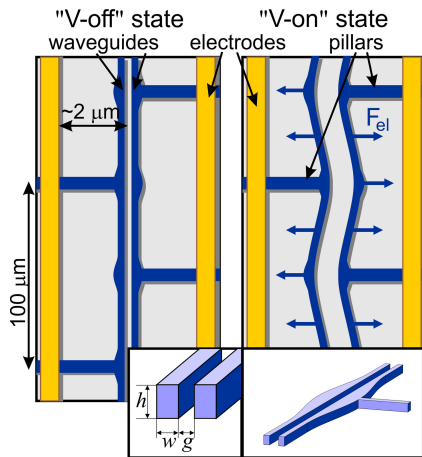


Fig. 1. Schematic geometry of the optical buffer (top view, not to scale) in the “voltage-off” (left) and “ON” (right) state. The waveguides are fixed at the pillars, and the electrostatic force ( $F_{el}$ , indicated by blue arrows) causes repulsion between the waveguides. Insets show 3-D images of coupled optical waveguides of height  $h$ , width  $w$  separated by an air gap  $g$  and S-shaped taper at the pillar connection point.

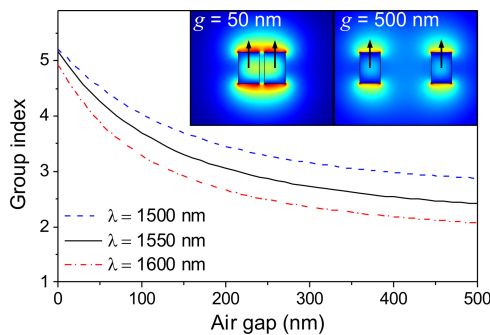


Fig. 2. Group index for the symmetric TE supermode as a function of the air gap  $g$  between coupled optical waveguides of dimensions  $195 \text{ nm} \times 300 \text{ nm}$ . Insets show the symmetric TE mode profile for  $g = 50 \text{ nm}$  and  $g = 500 \text{ nm}$ . Arrows show the predominant polarization.

parallel in the “voltage-off” state, and are bent upon application of a field. The alternating positions of the pillars ensure that the waveguides bend in a way to create a periodic structure with more or less uniform separation over their whole length, as will be shown in Section IV. The design of the pillars and the electrostatic actuation of the waveguides using MEMS techniques will be discussed in more detail in Sections III and IV, respectively.

The operating principle of the buffer was proposed in our previous work [5], in which we demonstrated the possibility of continuous variation of the group velocity, and hence of the signal propagation time, in dual suspended optical waveguides by varying the distance  $g$  between them. Here, we only briefly summarize the main points and optimize the design for InP. By maximizing the group index contrast using the method described in [5], we find optimum waveguide dimensions of  $195 \text{ nm} \times 300 \text{ nm}$  for operation in the TE mode. The dependence of the group index on the air gap width ( $g$ ) for the symmetric TE supermode (same phase of individual waveguide modes) is shown in Fig. 2. It should be stressed that for such small waveguides and air gaps the anti-symmetric modes ( $\pi$  phase shift between waveguides) do not exist because they are

cut-off, so light can only be launched simultaneously into both waveguides and propagates along the buffer without any power switching between individual waveguide. When the two waveguides are close together, a large fraction of the light propagates inside the waveguides, as shown in the inset in Fig. 2, leading to a large effective group index. When the air gap increases, the optical field spreads into the air around the waveguides, resulting in a lower effective group index, and hence faster propagation of an optical signal. A group index variation of 100% can be achieved when the separation between two waveguides changes by  $\sim 500 \text{ nm}$ . Fig. 2 shows data calculated for a spectral range of  $1500\text{--}1600 \text{ nm}$ , demonstrating that the device is capable of broadband operation. The  $100\text{nm}$  operating bandwidth is significantly wider than for optical buffers based on high-Q cavities and coupled resonator optical waveguides (CROW), where the operating bandwidth is typically less than  $1 \text{ nm}$  [2], [13], [14].

### III. WAVEGUIDE AND PILLAR SUPPORT DESIGNS

Signal delay time is proportional to the device length. From Fig. 2, continuous variation of optical delay time by up to  $\sim 10 \text{ ps}$  is expected in a  $1 \text{ mm}$  long device. In order to achieve longer delay times, a longer device is required. Minimizing propagation losses is therefore of paramount importance and various loss mechanisms will thus be considered in the following.

The first type of loss is caused by scattering of light by the surface roughness of the waveguides. The losses ranging from  $0.2$  to  $5 \text{ dB/cm}$  were reported for subwavelength silicon-on-insulator waveguides [15], [16], while the comparable losses of  $2.2 \text{ dB/cm}$  were measured in InP waveguides [17]. Theoretical models showed that these losses are proportional to the square of the standard deviation of the roughness and the square of the optical mode field on the rough surface [18]. As will be shown in Section V, the surface roughness for our device is mainly expected on the side walls as determined by the fabrication procedure, while the top and bottom surfaces are smooth with root mean square values of the surface roughness less than one nanometer. Thus, to minimize the scattering loss, we design a device to operate in the TE rather than TM mode, as this mode has weaker electric fields at the side walls [5].

Second, as was shown in Figs. 1 and 2, a significant fraction of light propagates in the air around the waveguides, which may lead to optical losses due to coupling to any nearby high index material. Due to the decay of the evanescent fields of the waveguides with distance, these losses are expected to depend exponentially on the waveguide separation from the bottom substrate and any side walls. Numerical simulations suggest that in order to keep the losses below  $0.1 \text{ dB/cm}$  and thus smaller than the surface roughness induced losses, each waveguide should be suspended  $>3 \mu\text{m}$  above the bottom substrate and  $>3 \mu\text{m}$  away from side walls.

The third type of losses occurs at pillar connections needed to support the waveguides. Pillars connected from the side interfere with the optical field causing additional scattering and leakage of light. To minimize these losses, the waveguides are designed with S-shaped tapers at the pillar intersections as shown schematically in the inset in Fig. 1. The light is confined more strongly inside the wide tapers, reducing the overlap

between waveguide mode and pillar [19], [20]. To optimize the taper dimensions and estimate losses, light propagation through a section of the waveguides with one pillar connection was modeled numerically using a finite element method (COMSOL Multiphysics) and an effective mode index method [21] to reduce the geometry of the problem to two dimensions. The taper shape was described by two sine-shaped lines allowing for a smooth connection with waveguides. A loss of  $\sim 0.2$  dB per pillar was calculated for the optimal taper of 600 nm width and length of 7–8  $\mu\text{m}$  in contrast to a loss  $>1$  dB per pillar found the case without a taper.

A pillar connected to one of the waveguides also introduces a phase shift of the propagated light. S-shaped sections were therefore designed on both waveguides at each pillar attachment point (see Fig. 1) to eliminate any relative phase delays between the waveguides.

#### IV. ELECTROSTATIC ACTUATION

The buffer operation is based on changing the separation between the two waveguides. In the following, we model the electrostatic actuation mechanism of the buffer. Actuation can be based on (i) reducing the air gap between two waveguides or (ii) separating two initially closely placed waveguides by applying voltages. The first operation principle suffers from a pull-in instability [22], in which elastic forces cannot counteract electrostatic forces beyond a certain threshold, which is likely to result in sticking of the waveguides. We thus concentrate on implementing the second actuation principle where sticking of the waveguides is avoided.

Two different electrostatic mechanisms which we call “passive” and “active” for the optical buffer actuation will be considered below.

In the passive method, waveguide actuation is achieved without direct electrical contacts to the waveguides via electrostatic forces [23], which are similar to dielectrophoretic forces widely used to manipulate micro-objects [24]. Charged electrodes on the chip are used to generate an electric field that polarizes the waveguides, creating electrostatic forces that are proportional to the gradient of the electric field squared [23]. These forces and hence the induced waveguide displacement therefore scale with the square of the voltage applied to the electrodes.

The modeled geometry for the passive actuation method consists of two continuous electrodes along the waveguides deposited on additional pillars placed at a distance of around 2  $\mu\text{m}$  from the waveguides to eliminate interaction with the guided optical field (as schematically shown in Fig. 1 (top view) and Fig. 3 (vertical cross section)). The electrodes are both charged with the same polarity and the bottom substrate ( $\sim 3$   $\mu\text{m}$  below the waveguides) is grounded. Fig. 3 shows the electric potential and electric field direction around the waveguides calculated for +10 V applied to the electrodes. The electric field has a significant gradient around the waveguides, the direction of which is shown by arrows. The field distribution resembles a quadrupole field configuration, which was recently shown to be the best one for actuation of a dual-core fiber with MEMS functionality [23]. The electrostatic forces in this case pull the waveguides

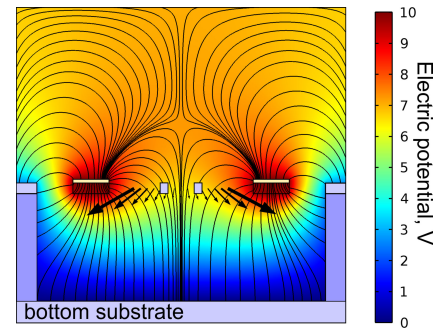


Fig. 3. Distribution of the electric field around the electrodes in the passive actuation method. The color indicates the electric potential. The lines indicate the direction of the electric field and the black arrows show the direction of the gradient of the electric field squared.

apart towards regions of stronger field, increasing the separation between them.

The second, active, method of electrostatic actuation relies on voltages being applied directly to the waveguides, hence no additional electrodes are required. In this case there is a direct interaction between the charged waveguides, and stronger interaction is expected than in the passive method which relies on induced electric dipole moments. Repulsion between the initially closely spaced waveguides can be achieved by applying the same voltage polarity to each, while the bottom substrate is again grounded.

The distance between two pillars,  $L$ , determines the mechanical properties of the waveguides. The waveguide maximum deformation caused by a unit force  $F$ , scales with the waveguide dimensions as  $\Delta g/F \sim L^3/(hw^3)$  [25]. The mechanical oscillation frequency is also determined by the waveguide dimensions as  $f_0 = \frac{5.6}{\pi} \frac{w}{L^2} \sqrt{\frac{E}{3\rho}}$  [25], where  $E$  is Young’s modulus and  $\rho$  the density of the waveguide material. For our chosen waveguide cross-section of 195 nm  $\times$  300 nm, an optimal distance between two pillars of 100  $\mu\text{m}$  ensures sufficient flexibility and high enough mechanical frequency ( $\sim 75$ –100 kHz) to reduce vibration noise. Simultaneously, this then suggests mechanical response times of the order of 10  $\mu\text{s}$  when actuating the device, which is of the same order of magnitude as the response time reported for other optical MEMS devices based on suspended waveguides [7], [9].

By combining the electrostatic models for the two actuation mechanisms with a model of the mechanical deformation of two identical freestanding waveguides supported by pillars as shown in Figs. 1 and 4, we calculated the deformations of each waveguide in the transverse direction and the shape of the air gap between the waveguides along the device length for a range of voltages applied to the electrodes or waveguides assuming 50 nm initial air gap and 100  $\mu\text{m}$  distance between pillars. Because the waveguides are of equal dimensions, the deformation amplitude of each waveguide is the same. The air gap increases upon actuation along the whole device length; its width has variations which are below 10% of the average air gaps in the studied voltage range and have periodicity of  $L/2$  as shown in Fig. 4. For example, for data shown in Fig. 4 the air gap variation is 26 nm and the average air gap is 276 nm. Moreover, this or larger variations are only observed at large air gaps where the

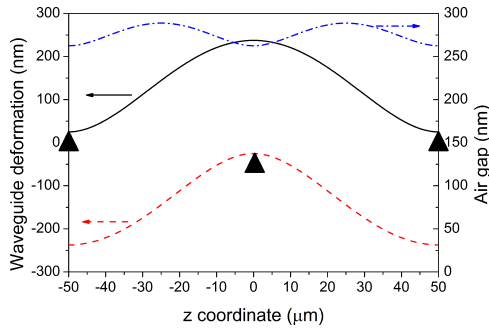


Fig. 4. (Left axis) Black (solid) and red (dash) lines show position of waveguides deformed in transverse direction along the buffer length. Triangles indicate pillar connection points. (Right axis) Blue line shows variation of the air gap between waveguides along the device. Both calculations were done for the “active” actuation method, assuming 2 V applied to the waveguides, 50 nm initial air gap, and 100  $\mu\text{m}$  distance between pillars.

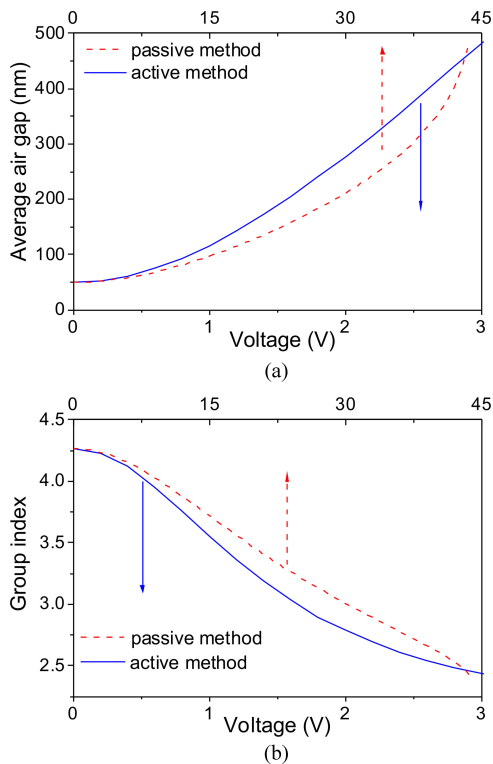


Fig. 5. (a) Variation of average gap and (b) group index depending on the voltage applied to the waveguides or electrodes in the case of passive or active actuation method, respectively.

group index is not very sensitive to the gaps, so this should not affect the device performance. However, for waveguides with non-identical cross-sections, larger variations in the air gap profile and thus on average smaller effective index tunability are expected.

The average air gap calculated for the passive and active methods are compared in Fig. 5(a). For the passive method, an increase of air gap from 50 to 500 nm is predicted with a driving voltage of  $\sim 45$  V, above which a pull-in instability occurs and the waveguides collapse onto the electrodes. By contrast, a driving voltage of only 3 V is required for the active method. Moreover, no pull-in instability exists with this method. Fig. 5(b) shows the group refractive index dependence on the

0.3 $\mu\text{m}$ InGaP (Device Layer)
4 $\mu\text{m}$ InGaAs (Sacrificial Layer)
n-type InP Substrate

Fig. 6. Schematic diagram of the sample layer structure of the InP MEMS waveguides device.

voltage in the case of passive and active methods. Up to 100% variation of the group index is expected, which corresponds to a variation of delay time by  $\sim 10$  ps in a 1 mm long device.

To apply voltages to the waveguide in the active method, the waveguide material has to be doped to enable electrical conductivity. This creates additional optical losses due to free-carrier absorption. Using the method described in [26], we estimated the losses for n-type doped InP with a doping concentration of  $n = 5 \times 10^{17} \text{ cm}^{-3}$  to be  $\sim 2.5$  dB/cm which is of the order of the expected propagation losses due to sidewall roughness and should therefore be acceptable for the device.

## V. SAMPLE STRUCTURE AND CHARACTERIZATION

The InP optical buffer structure was grown on an n-type InP substrate by molecular beam epitaxy (MBE). A 4  $\mu\text{m}$  layer of  $\text{In}_{0.53}\text{Ga}_{0.47}\text{As}$  was grown on the InP substrate first, followed by a 300 nm device layer of  $\text{In}_{0.99}\text{Ga}_{0.01}\text{P}$  (i.e., 1% of Ga in InP). The layer structure of the sample is shown schematically in Fig. 6. The InGaAs layer served as a sacrificial layer to be etched away at a later stage of the fabrication process when releasing the waveguide structure. A small percentage of Ga was introduced to the device layer in order to provide slight tension to the waveguides. This helps to prevent the waveguides collapsing after the waveguide release step.

As discussed in Section III, it is important to obtain a smooth InGaP device layer surface in order to minimize optical losses through surface scattering. We therefore investigated the surface quality of the top InGaP layer by atomic force microscopy (Bruker dimension icon) [27], [28]. 3-D and 2-D AFM topography images of the InGaP layer imaged in tapping mode are presented in Fig. 7(a) and (b), respectively. The area scanned was  $5 \mu\text{m} \times 5 \mu\text{m}$ , and multiple areas were scanned at different parts of the wafer to ensure that our data gave a true representation of the surface quality across the whole wafer. Our image analysis showed the maximum height difference was typically  $5 \pm 2$  nm, and the root mean square value of the surface roughness ( $R_q$ ) was typically  $0.61 \pm 0.10$  nm. These values indicate the surface of our epitaxially grown InGaP layer was very smooth.

We also investigated the surface quality of the InGaAs sacrificial layer. This is important as it provides an indication of the quality of the bottom surface of the InGaP device layer. To investigate this, a 4  $\mu\text{m}$  layer of InGaAs was grown on an InP substrate under the same growth conditions as those used for the complete optical buffer structure. Our AFM image analysis yield an average rms value of the surface roughness of  $0.376 \pm 0.04$  nm, and typical maximum height difference was  $3.2 \pm 0.4$  nm. This indicates that the interface between the InGaAs and InGaP was also very smooth.

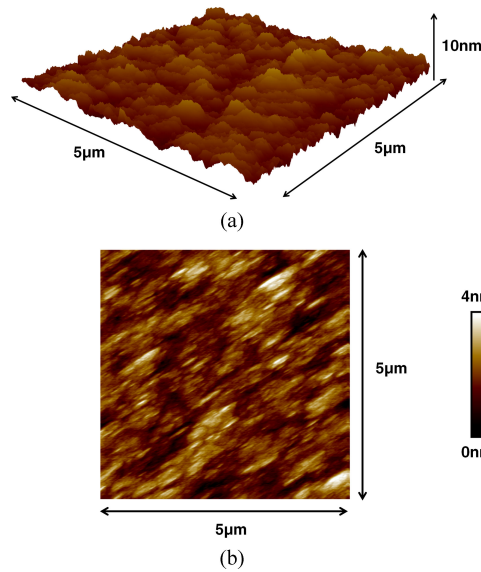


Fig. 7. (a) 3-D and (b) 2-D AFM topographic image of the InGaP device layer surface measured in tapping mode.

## VI. FABRICATION

A device designed for “active” electrostatic actuation (see Section IV) was fabricated on a  $1\text{ cm} \times 1\text{ cm}$  InP chip. Following deposition of the  $\text{In}_{0.53}\text{Ga}_{0.47}\text{As}$  sacrificial layer, an InGaP device layer was grown, from which the waveguides, supporting side pillars and metal contact pads were fabricated.

Metal contact electrode pads were required in order to provide voltage to the waveguides. The areas of the electrode pads were patterned by electron beam lithography (Raith150-TWO). Cr/Au contacts were subsequently deposited by thermal evaporation and lift-off in acetone.

Patterning of the parallel waveguides was carried out using hydrogen silsesquioxane electron beam resist as a negative mask. The dimensions of the patterned waveguides were  $250\text{ nm}$  width and  $200\text{ }\mu\text{m}$  length. The spacing between the waveguides was approximately  $300\text{ nm}$ . Pillars were patterned in the same step as the waveguides. In the first generation of devices, a pillar spacing of  $40\text{ }\mu\text{m}$  was chosen as a starting point for our initial fabrication work. This increased the number of pillars along the waveguide structure and it helped us to check the uniformity of the pillar supports at different parts of the waveguides. In future work the pillar spacing will be increased to  $100\text{ }\mu\text{m}$  to match the design as discussed in Section IV. Each pillar was composed of two parts: An S-shaped area that attached to the waveguide and a rectangular section that linked the S-shaped area to the large contact pad. The length of the S-shaped area was approximately  $5\text{ }\mu\text{m}$  and the width was  $500\text{ nm}$ . The length of the rectangular section was  $3\text{ }\mu\text{m}$ . Pillar positions on the waveguides were staggered to allow the waveguides to be pulled apart by the applied field. A section of the pattern is shown in Fig. 8(a).

After the patterning of the waveguides and pillars on the device layer, the structure was etched by reactive ion etching (RIE) with a cyclic methane-hydrogen/oxygen plasma. The resulting etched structure had a sidewall angle better than  $80^\circ$  (see Fig. 8(b)). After the RIE etch, the waveguides were released us-

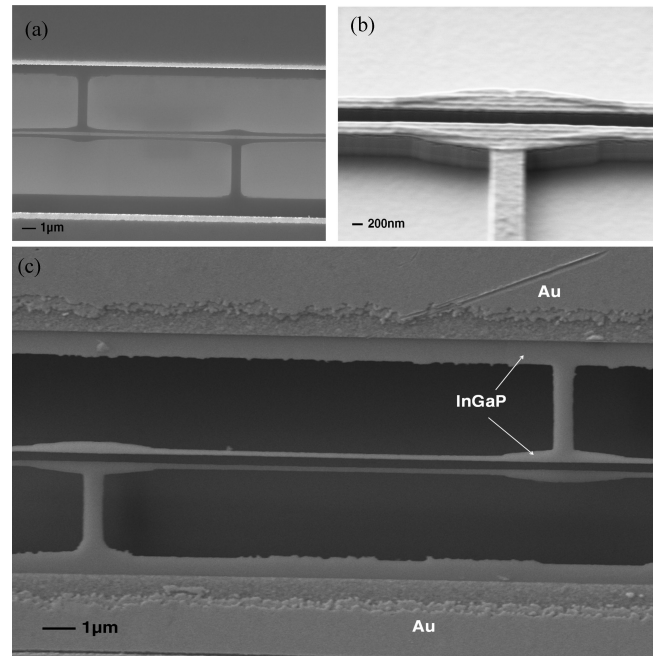


Fig. 8. SEM images of (a) top view of the waveguide and pillar pattern after electron beam lithography, (b) side view of the reactive ion etched pillar section of the structure, and (c) top view of waveguides and pillar supports after HF etch. Surfaces of InGaP waveguides and pillars were smooth after the waveguide release step. The gold and waveguide layers are indicated in the image.

ing  $\text{HF}:\text{H}_2\text{O}_2:\text{H}_2\text{O}$  (1:1:8) solution. This step etched away the InGaAs layer and the etch mask cleanly, without leaving any residual resist on the waveguide surfaces. The released waveguides structure was dried using supercritical  $\text{CO}_2$  in order to avoid stiction.

The sample substrate was cleaved to the same length as the suspended waveguides using an automated wafer scribe. This will help to facilitate the coupling of a free space beam into the waveguides for optical testing. We have not yet tested the quality of the etched facets. However, if required, the facet quality could be improved by polishing with a focused ion beam. For a further decrease in insertion loss, a tapered coupler can be designed at the input and output facets.

Fig. 8(c) shows an SEM image of the released waveguide and pillar support structure. The dimensions of each waveguide were approximately  $300\text{ nm}$  (height)  $\times$   $200\text{ nm}$  (width)  $\times$   $200\text{ }\mu\text{m}$  (length). The spacing between the waveguides was approximately  $400\text{ nm}$ . The suspended waveguides and pillar supports did not collapse after the waveguide release step.

The dimensions of the fabricated waveguides were comparable with the designed dimensions. However, the air gap between the waveguide was  $400\text{ nm}$ , which was significantly wider than the  $300\text{ nm}$  patterned gap after the electron beam lithography step. The increase in air gap is due to the side wall etching of waveguides during RIE. This can be corrected by adjusting the width and position of the waveguides in the lithography pattern design. Controlling the size of the air gap during fabrication is very critical for the device function. If it is too narrow, the waveguides are likely to have stiction during actuation and they would become very hard to separate. If the gap is too wide, the

waveguides are too far apart to achieve strong optical coupling and the structure would not function as a tunable optical buffer.

It is also important to control the dimensions of the waveguides. If they are too wide, the optical mode would be guided in the individual waveguides rather than the combination of waveguides and air gap. If they are too narrow, the change of refractive index experienced by the optical mode would not be as much as predicted, and the structure would also become more fragile.

## VII. CONCLUSION

We have demonstrated the fabrication of long suspended dual-waveguide structures of submicron ( $200 \text{ nm} \times 300 \text{ nm}$ ) transverse dimensions in the InP platform. These structures are suitable for the realization of MEMS-actuated optoelectronic devices integrated monolithically with lasers, amplifiers, and other optical components on a single chip for optical telecommunication applications. The fabricated waveguides exhibited a side wall profile better than  $80^\circ$ . For our MBE grown InGaP waveguides on InP substrate structure, the AFM data show that the surface of the InGaP and InGaAs layers are very smooth with rms roughness values of less than 1 nm, which helps to minimize optical loss through scattering.

The fabricated device is based on the design for a continuously tunable optical buffer with MEMS actuation. Our simulations showed that up to 100% group index variation can be achieved when the separation between the two waveguides changes by  $\sim 500 \text{ nm}$ . Different options for electrostatic actuation were studied numerically and the design was optimized for low optical losses, sufficient mechanical stability, and broadband operation. We estimate that our optical buffer structure can achieve a continuous optical delay time of  $\sim 10 \text{ ps}$  for a 1 mm long device. Although other designs based on high-Q cavities and CROW can achieve longer delays with smaller device sizes, their operating bandwidth is much narrower than for our approach.

Future work will focus on improving the fabricated device dimensions to match more closely with the design, especially narrowing the spacing between the waveguides, and demonstrating its full functionality as an optical buffer.

## REFERENCES

- [1] R. Langenhorst *et al.*, "Fiber loop optical buffer," *J. Lightw. Technol.*, vol. 14, no. 3, pp. 324–335, Mar. 1996.
- [2] F. Xia, L. Sekaric, and Y. Vlasov, "Ultracompact optical buffers on a silicon chip," *Nature Photon.*, vol. 1, pp. 65–71, 2007.
- [3] J. B. Khurgin, "Optical buffers based on slow light in electromagnetically induced transparent media and coupled resonant structures: A comparative analysis," *J. Opt. Soc. Amer. B*, vol. 22, pp. 1062–1074, 2005.
- [4] A. H. Safavi-Naeini *et al.*, "Electromagnetically-induced transparency and slow light with optomechanics," *Nature*, vol. 472, pp. 69–73, 2011.
- [5] P. Horak, W. Stewart, and W. H. Loh, "Continuously tunable optical buffer with a dual silicon waveguide design," *Opt. Exp.*, vol. 19, pp. 12456–12461, 2011.
- [6] T. Ikeda, K. Takahashi, Y. Kanamori, and K. Hane, "Phase-shifter using submicron silicon waveguide couplers with ultra-small electro-mechanical actuator," *Opt. Exp.*, vol. 18, pp. 7031–7037, 2010.
- [7] Y. Akihama and K. Hane, "Single and multiple optical switches that use freestanding silicon nanowire waveguide couplers," *Light Sci. Appl.*, vol. 1, e16, pp. 1–8, 2012.
- [8] E. Ollier, "Optical MEMS devices based on moving waveguides," *IEEE J. Sel. Topics Quantum Electron.*, vol. 8, no. 1, pp. 155–162, Jan./Feb. 2002.
- [9] M. W. Pruessner *et al.*, "InP-based optical waveguide MEMS switches with evanescent coupling mechanism," *J. Microelectromech. Syst.*, vol. 14, pp. 1070–1081, 2005.
- [10] F. Lelarge *et al.*, "Recent advances on InAs/InP quantum dash based semiconductor lasers and optical amplifiers operating at  $1.55 \mu\text{m}$ ," *IEEE J. Sel. Topics Quantum Electron.*, vol. 13, no. 1, pp. 111–124, Jan./Feb. 2007.
- [11] W. H. Ng *et al.*, "Broadband quantum cascade laser emitting from 7.7 to  $8.4 \mu\text{m}$  operating up to 340K," *J. Appl. Phys.*, vol. 101, p. 046103, 2007.
- [12] J. B. D. Soole and H. Schumacher, "InGaAs metal-semiconductor-metal photodetectors for long wavelength optical communications," *IEEE J. Quantum Electron.*, vol. 27, no. 3, pp. 737–752, Mar. 1991.
- [13] J. K. S. Poon, L. Zhu, G. A. DeRose, and A. Yariv, "Transmission and group delay of microring coupled-resonator optical waveguides," *Opt. Lett.*, vol. 31, pp. 456–458, 2006.
- [14] S. Manipatruni, C. B. Poitras, Q. Xu, and M. Lipson, "High-speed electro-optic control of the optical quality factor of a silicon microcavity," *Opt. Lett.*, vol. 33, pp. 1644–1646, 2008.
- [15] Y. A. Vlasov and S. J. McNab, "Losses in single-mode silicon-on-insulator strip waveguides and bends," *Opt. Exp.*, vol. 12, no. 8, pp. 1622–1631, 2004.
- [16] M. Lipson, "Guiding, modulating, and emitting light on silicon—challenges and opportunities," *J. Lightw. Technol.*, vol. 23, no. 12, pp. 4222–4238, Dec. 2005.
- [17] D. Kelly *et al.*, "Monolithic suspended optical waveguides for InP MEMS," *IEEE Photon. Technol. Lett.*, vol. 16, no. 5, pp. 1298–1300, May 2004.
- [18] F. P. Payne and J. P. R. Lacey, "A theoretical analysis of scattering loss from planar optical waveguides," *Opt. Quantum Electron.*, vol. 26, pp. 977–986, 1994.
- [19] T. Fukazawa, T. Hirano, F. Ohno, and T. Baba, "Low loss intersection of Si photonic wire waveguides," *Jpn. J. Appl. Phys.*, vol. 43, no. 2, pp. 646–647, 2004.
- [20] L. Martinez and M. Lipson, "High confinement suspended microring resonators in silicon-on-insulator," *Opt. Exp.*, vol. 14, no. 13, pp. 6259–6263, 2006.
- [21] K. Okamoto, "Effective index method," in *Fundamentals of Optical Waveguides*, 2nd ed. Amsterdam, The Netherlands: Elsevier, 2006, pp. 37–40.
- [22] W.-M. Zhang, H. Yan, Z.-K. Peng, and G. Meng, "Electrostatic pull-in instability in MEMS/NEMS: A review," *Sensor Actuat. A, Phys.*, vol. 214, pp. 187–218, 2014.
- [23] N. Podoliak, Z. Lian, W. H. Loh, and P. Horak, "Design of dual-core optical fibers with NEMS functionality," *Opt. Exp.*, vol. 22, pp. 1065–1076, 2014.
- [24] T. B. Jones, *Electromechanics of Particles*. Cambridge, U.K.: Cambridge Univ. Press, 1995.
- [25] V. Kaajakari, "Beams as micromechanical springs," in *Practical MEMS*. New York, NY, USA: Small Gear Publishing, 2009.
- [26] J. M. Ziman, "Optical properties," in *Principles of the Theory of Solids*, 2nd ed. Cambridge, U.K.: Cambridge Univ. Press, 1972, pp. 255–291.
- [27] G. Binnig and S. F. Quate, "Atomic force microscope," *Phys. Rev. Lett.*, vol. 56, pp. 930–933, 1986.
- [28] Y. Martin, C. C. Williams, and H. K. Wickramasinghe, "Atomic force microscope-force mapping and profiling on a sub  $100\text{-\AA}$  scale," *J. Appl. Phys.*, vol. 61, pp. 4723–4729, 1987.



**Wing H. Ng** received the M.Sc. degree in physics from the University of Durham, Durham, U.K., in 2001, the M.Sc. degree in optics and photonics from Imperial College London, London, U.K., in 2002, and the Ph.D. degree in semiconductor physics from the University of Sheffield, Sheffield, U.K., in 2007.

He was with the photonics industry for a number of years after receiving the Ph.D. degree. He joined the Department of Electronic and Electrical Engineering at University College London, London, in 2013, where he is currently a Research Associate. His research interests include nanofabrication of semiconductor structures, optoelectronic devices, photonic integrated circuits, and resistive switching in  $\text{SiO}_2$  and polymer-based materials.

Dr. Ng is a Member of the Institute of Engineering and Technology (U.K.), and the Institute of Physics (U.K.).



**Nina Podoliak** received the M.Sc. degree in theoretical physics from Kiev National University, Kyiv, Ukraine, in 2008, and the Ph.D. degree in physics from the University of Southampton, Southampton, U.K., in 2012.

Since 2012, she has been a Postdoctoral Research Fellow with the Optoelectronics Research Centre, University of Southampton. Her current research interests include design and optimization of optical micro- and nanoelectromechanical systems for telecommunication applications and modeling of

light propagation in optical fibers and plasmonic waveguides.



**William J. Stewart** was educated at Imperial College London, London, U.K.

He was a Chief Scientist at Marconi, and currently he is a Visiting Professor at University College London, and the Optoelectronics Research Centre, University of Southampton, Southampton, U.K. His research interests include nanomechanical photonics, photonic crystals, optical slow-wave structures, metamaterials, inkjet printing of glasses, and the application of various optical, semiconductor, and acoustic technologies to medicine, particle physics, and industrial processes.

He is the author of more than 65 conference and journal papers, including many invited papers, and more than 50 patents.

Prof. Stewart is a Fellow of the Royal Academy of Engineering, the Institute of Physics, the Institute of Engineering and Technology, and the Optical Society of America. He is a past Member of the editorial advisory board for the journal "Science," and the Chair of the U.K. IET's Communications Sector panel. He is also a Member of the U.K. Government's Engineering Infrastructure Expert Group.



**Peter Horak** received the M.Sc. and Ph.D. degrees in theoretical physics from the University of Innsbruck, Innsbruck, Austria, in 1993 and 1997, respectively. Since 2001, he has been with the Optoelectronics Research Centre, University of Southampton, Southampton, U.K. His research interests include the theoretical and numerical investigation of photonic devices, including linear, nonlinear, and quantum optical effects.

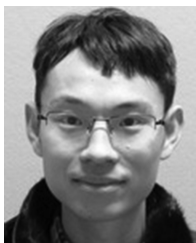


**Anthony J. Kenyon** (M'08–SM'14) received the B.Sc. and D.Phil. degrees in chemical physics from the University of Sussex, Brighton, U.K. in 1986 and 1992, respectively.

He joined the Electronic and Electrical Engineering Department of University College London, London, U.K., in 1992, where he currently holds the position of Professor of nanoelectronic and nanophotonic materials. His research interests include nanostructured materials for electronics and photonics, silicon photonics, resistive switching, and self-assembled

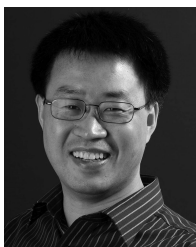
nanoscale systems. He is the author of more than 80 peer-reviewed publications, and is on the editorial board of several journals.

Prof. Kenyon is a Fellow of the Institute of Physics and the Institute of Engineering and Technology and serves on the Board of Delegates of the European Materials Research Society. He regularly gives invited talks at major international meetings, and has coorganized a number of international symposia.



**Jiang Wu** received the B.S. degree from the University of Electronic Science and Technology of China, Chengdu, China, and the M.S. and Ph.D. degrees from the University of Arkansas-Fayetteville, Fayetteville, AR, USA, in 2008 and 2011, respectively.

He is currently a Research Associate in the Department of Electrical and Electronic Engineering at University College London, London, U.K. His research interests include molecular beam epitaxy growth and optoelectronic devices, including photovoltaic cells, lasers, and photodetectors.



**Huiyun Liu** received the Ph.D. degree in semiconductor science from the Institute of Semiconductor, Chinese Academy of Sciences, Beijing, China.

After receiving the Ph.D. degree, he joined the EP-SRC National Center for III–V Technologies at the University of Sheffield, Sheffield, U.K., in August 2001. In 2007, he received Royal Society University Research Fellow and joined the Department of Electronic and Electrical Engineering at University College London, London, U.K., where he is currently a Professor of Semiconductor Photonics. He has published

more than 120 peer-reviewed papers on developing III–V compound materials and devices. His current research interests include the nanometer-scale engineering of low-dimensional semiconductor structures (such as quantum dots, nanowires, and quantum wells) by using molecular beam epitaxy and the development of novel optoelectronic devices including lasers, detectors, and modulators by developing novel device process techniques.